Volume 14
Number 14
21 July 2024
Pages 3809–4076

Catalysis Science & Technology

rsc.li/catalysis

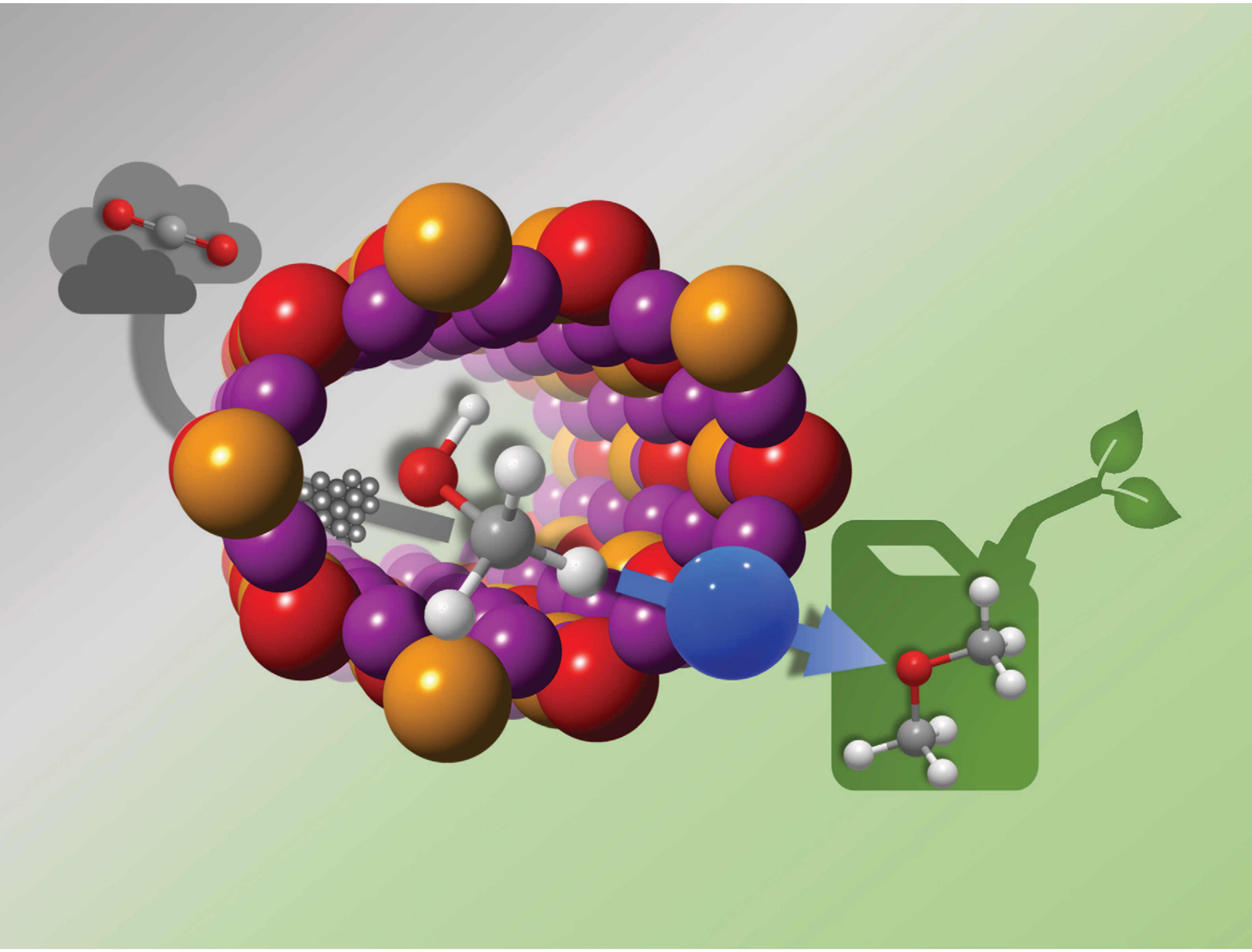

ISSN 2044-4761

ROYAL SOCIETY
OF **CHEMISTRY**

PAPER
Robert Raja *et al.*
Designing bifunctional catalysts for the one-pot conversion of CO_2 to sustainable marine transportation fuels

Catalysis
Science &
Technology

ROYAL SOCIETY
OF CHEMISTRY

PAPER

Cite this: *Catal. Sci. Technol.*, 2024, **14**, 3853

Designing bifunctional catalysts for the one-pot conversion of CO_2 to sustainable marine transportation fuels†

Maciej G. Walerowski, [a] Matthew E. Potter, [bcd] Elizabeth S. Burke, [a] Stylianos Kyrimis, [e] Lindsay-Marie Armstrong [e] and Robert Raja *[a]

Received 8th January 2024,
Accepted 2nd April 2024

DOI: 10.1039/d4cy00020j

rsc.li/catalysis

Meeting ambitious net-zero targets will require the replacement of marine fossil fuels with sustainable alternatives such as dimethyl ether (DME). DME is non-toxic, can be fully produced *via* a circular carbon economy and can be rapidly deployed due to its compatibility with existing liquid petroleum gas infrastructure. One-pot production of DME from CO_2 *via* a methanol intermediate is achieved by combining redox and Brønsted or Lewis acid sites. Herein, we have synthesised, characterised and tested a variety of bifunctional CuZnO/silicoaluminophosphate catalysts for the one-pot production of DME. A range of synthetic approaches were employed to combine the redox and acidic functionalities in order to derive synthesis–structure–property correlations to guide the design of improved catalysts. We found that a CuZnO/SAPO-34 catalyst made *via* impregnation and drying can achieve 80% DME selectivity with no detectable toxic CO by-product formation. High acid site abundance resulted in extensive dehydration of the intermediate methanol, which increased localised water production, suppressing the CO-forming reverse water gas shift reaction and thus yielding exceptional DME selectivity that is amongst the highest in literature.

Introduction

Alternative fuels such as hydrogen have been touted as sustainable options for the marine sector, however deployment of these fuels will require significant propulsion and infrastructure overhaul and are therefore seen as medium-to-long term solutions.[1–3] In the short-to-medium term, sustainable 'drop in' fuels are required. These fuels should be compatible with existing vessels and infrastructure to enable their rapid deployment without the need for significant retrofitting. Dimethyl ether (DME) is a promising alternative to marine diesel as it is not toxic, corrosive nor carcinogenic and can be produced using a circular carbon economy making it potentially a carbon-neutral fuel. DME also has a higher cetane number than diesel so will burn more effectively within a compression engine, moreover its physical properties are similar to liquid petroleum gas so existing infrastructure can be utilised for rapid deployment.[4–7] In recognition of this, the global DME market is projected to double from \$4.1 billion in 2021 to \$8.8 billion by 2030.[8] DME can be produced *via* a two-pot or one-pot (eqn (1))[7] approach from either syngas (CO, CO_2 and H_2 mixture) or CO_2 and H_2 mixture.[5,7,9,10]

$$2CO_2 + 6H_2 \leftrightarrow CH_3OCH_3 + 3H_2O\ (\Delta H_{298K} = -123\ \text{kJ mol}^{-1}) \quad (1)$$

In the two-pot approach commercialised by firms such as Toyo (Table 1),[11] the established methanol (MeOH) synthesis process uses a Cu-based catalyst, *e.g.* $Cu/ZnO/Al_2O_3$ to convert syngas to MeOH (eqn (2))[12] which is separated, purified and subsequently dehydrated (eqn (3))[7] in a separate reactor with a solid acid catalyst such as a zeolite or γ-Al_2O_3 to give the desired DME.

$$CO + 2H_2 \leftrightarrow CH_3OH\ (\Delta H_{298K} = -90.7\ \text{kJ mol}^{-1}) \quad (2)$$

$$2CH_3OH \leftrightarrow CH_3OCH_3 + H_2O\ (\Delta H_{298K} = -23.4\ \text{kJ mol}^{-1}) \quad (3)$$

Selective dehydration of MeOH to DME is favoured by weak and moderate acid sites as strong acid sites can over dehydrate MeOH to give olefins or coke.[5,9,13–15] As zeolites (*e.g.* ZSM-5) often have strong acid sites, alkali ion modification is usually undertaken to temper acidity and boost DME selectivity.[5,13,16,17] Aluminophosphates are

---

[a] *School of Chemistry, University of Southampton, Southampton, SO17 1BJ, UK. E-mail: R.Raja@soton.ac.uk*
[b] *Chemistry Department, University College London, London, WC1E 6BT, UK*
[c] *UK Catalysis Hub, Harwell Research Complex, Harwell, OX11 0FA, UK*
[d] *Department of Chemistry, University of Bath, Bath, BA2 7AY, UK*
[e] *School of Engineering, University of Southampton, Southampton, SO17 1BJ, UK*

† Electronic supplementary information (ESI) available. See DOI: **https://doi.org/10.1039/d4cy00020j**

Table 1 Overview of different DME production plants

Process	Firm	Launch date	Output (tons per year)	Location	Ref.
Two-pot	Toyo	2007	210 000	Lingwu, China	21
Two-pot	MGC, JGC, Grillo	2012	20 000	Frankfurt, Germany	22
One-pot	KOGAS	2008	3600	Incheon, Korea	23
One-pot	MGC, MC, MHIENG	2020	20 000	La Brea, Trinidad & Tobago	24

analogues to zeolites where the framework is built from PO_4 and AlO_4 tetrahedra, which link together to give diverse topologies. Substitution of framework P^{5+} for Si^{4+} gives rise to charge balancing Brønsted acid sites (which can act as the active sites for MeOH dehydration), leading to the formation of silicoaluminophosphates (SAPOs).[18,19] Bonding in SAPOs is more ionic in nature compared to zeolites which leads to greater charge localisation resulting in stronger interactions between Brønsted acidic protons and framework oxygens. This results in weaker acid strength of SAPOs making them well-suited for selective dehydration of MeOH to DME.[18,20]

In a one-pot approach, both the MeOH synthesis and subsequent MeOH dehydration reactions occur in one reactor using either a mixture of two distinct catalysts, or with a singular bifunctional catalyst which contains both redox and acid sites.[5,7] The one-pot approach has a number of benefits over the traditional two-pot method. Firstly, there are large financial and engineering advantages as a singular reactor is required and the intermediate MeOH purification and separation steps are removed.[9] The initial MeOH synthesis reaction itself is challenging as usually it involves two distinct reactions: CO_2 hydrogenation to MeOH (eqn (4))[13] and the reverse water gas shift (RWGS) reaction (eqn (5))[7,12] to form CO with their equilibrium determining the final MeOH product yield.

$$CO_2 + 3H_2 \leftrightarrow CH_3OH + H_2O\ (\Delta H_{298K} = -49.5\ \text{kJ mol}^{-1}) \quad (4)$$

$$CO_2 + H_2 \leftrightarrow CO + H_2O\ (\Delta H_{298K} = 41.2\ \text{kJ mol}^{-1}) \quad (5)$$

From a reaction perspective therefore, the immediate dehydration of MeOH as it is formed is thermodynamically favourable as conversion of MeOH to DME can shift the equilibrium towards further MeOH production (eqn (4)) which can increase the overall CO_2 conversion.[5,7,9,10] Moreover, dehydration of MeOH as it is formed can also help to suppress the parasitic RWGS reaction which produces the undesirable, highly toxic CO by-product.[25–27] This is possibly due to increased water production which can shift the equilibrium away from CO formation (eqn (5)). However, one-pot conversion of CO_2 to DME requires the design of highly active, selective and stable bifunctional catalysts which is not a trivial task as embedding two active sites (Fig. 1) into one catalyst is challenging, running the risk of impacting the performance of the individual sites. Significant research effort has gone into developing catalysts for the one-pot conversion of CO_2 or syngas to DME (Fig. S1†).[7,10]

As discussed previously, SAPO based bifunctional catalyst could give high DME selectivity due to their weaker strength acid sites. Yoo *et al.* have created a series of physical mixture (PM) catalysts by mixing $Cu/ZnO/Al_2O_3$ catalyst with different SAPO solid acid catalysts for the one-pot conversion of syngas to DME.[28] They found that solid acids with stronger acid sites such as SAPO-18 and SAPO-34 had higher initial activity for conversion of syngas to DME but these deactivate rapidly due to the formation of pore plugging coke whereas the contrary was true for SAPO-5 and SAPO-11 which had weaker acid sites. Navarro-Jaén *et al.* have also developed a series of PM catalysts by mixing $Cu–ZnO–M_xO_y$ (where M = Al, Zr or Ce) with SAPO-34, but the catalyst was used for the conversion of CO_2, rather than syngas, to DME.[29] Although the $Cu–ZnO–Al_2O_3$/SAPO-34 PM catalyst had high CO_2 conversion of 19.8%, its CO selectivity was very high (70.9%) emphasising the difficulty in using PM catalysts for the one-pot production of DME. Yao *et al.* investigated whether this high CO selectivity could be suppressed by combining SAPO-34 and Cu–In–Zr–O catalysts in different integration manners to give catalyst beds with varying proximity between the two functionalities. The best catalyst achieved 4.3% CO_2 conversion and 65.1% DME selectivity at 250 °C and 30 bars.[26] It was shown that more intimate contact between the two catalysts (*e.g.* powder *vs.* pellet/granule mixing) gave higher CO_2 conversions and DME selectivity, which suggested

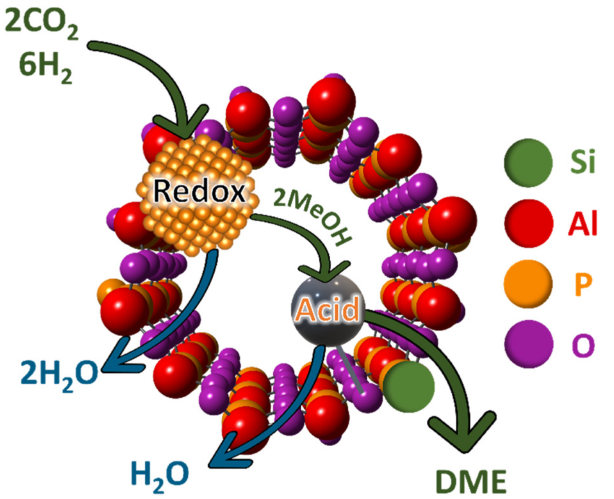

Fig. 1 Graphical representation of a microporous SAPO pore, containing a redox site (combination of Cu and ZnO), and an acidic site (Brønsted acid site), performing the one-step formation of DME from CO_2 and H_2, through a cascade pathway.

that bringing redox and acid active sites closer might suppress the RWGS reaction. Core–shell catalysts such as $Cu–ZnO–Al_2O_3@SiO_2–Al_2O_3$ have been developed as a single bifunctional catalyst for the one-pot conversion of CO_2 to DME.[30] By enveloping the Cu-based catalyst in a mesoporous acidic shell, it was possible to retain the active Cu^0–ZnO interface which increased MeOH + DME selectivity (from 9.1 to 63.3 mol%) and significantly tempered, although not fully eliminated, the formation of CO. This suggested that controlling active site proximity can be used to optimise product selectivity, something which not possible with a PM system or in a two-pot approach. Bahruji *et al.*[27] and Tariq *et al.*[31] have used chemical vapour impregnation (CVI) to deposit PdZn and CuZnO nanoparticles onto the zeolite ZSM-5, respectively, to create integrated bifunctional catalysts for conversion of CO_2 to DME. Through electron microscopy, they found that by using CVI, it is possible to decorate the outer crystal faces of the solid acid with uniformly distributed metallic nanoparticles, thus achieving high proximity between redox and acid active sites. Here a low DME selectivity was achieved and this was attributed to blocking of the Brønsted acid sites by the metallic nanoparticles. Bahruji *et al.* did however find that subsequent dehydration of MeOH can suppress the parasitic RWGS reaction and decrease the selectivity for CO during one-pot conversion of CO_2 to DME.[27] Based on these works, a highly active and selective bifunctional catalyst for the one-pot conversion of CO_2 to DME requires a weakly acidic functionality, proximity between the redox and acid active sites and a high dispersion and anchorage of the redox functionality.

A diverse array of catalytic candidates have been synthesised using various methods for the one-pot synthesis of DME from either syngas or CO_2. A number of works explored the impact of the synthesis method or precursor identity on the structure and performance of bifunctional catalysts.[5,32–35] However, these studies have focused on the one-pot conversion of syngas to DME rather than CO_2 and H_2 to DME and mostly utilised commercially available zeolite ZSM-5 or γ-Al_2O_3 as the acidic functionality which, as already discussed, may not be the most suitable acidic functionality. Herein, we have developed a series of bifunctional CuZnO/SAPO-11 and CuZnO/SAPO-34 catalysts using different preparation methods to develop holistic synthesis–structure–property correlations (SSPCs). SAPO-11 and SAPO-34 were chosen as they have contrasting acid strengths, textural properties, morphologies and topologies. A range of wet chemistry methods were used to combine CuZnO with SAPO-11 or SAPO-34 to understand the interplay between synthesis, structure and performance. We have demonstrated that by tailoring the synthesis method, it is possible to obtain synergy between Cu and ZnO sites as well as interaction between these species and the solid acid support. Through careful choice of synthesis approach we were able to deposit the CuZnO nanoparticles directly onto the SAPO support surface which resulted in instantaneous dehydration of MeOH giving CO_2 conversions of 8%, high DME selectivity of 80% and no detectable CO due to significant suppression of the parasitic RWGS reaction.

Experimental

Catalyst synthesis and characterisation

SAPO-11 and SAPO-34 were synthesised according to published hydrothermal approaches, described in section 1.1 of the ESI.†[36,37] Several methods were tested to synthesise the CuZnO/SAPO-11 and CuZnO/SAPO-34 bifunctional catalysts, specifically impregnation and drying (ID), oxalate gel precipitation deposition (OG) and deposition precipitation (DP) methods. The CuZnO/SAPO-11 and CuZnO/SAPO-34 bifunctional catalysts were tested against SAPO-11 or SAPO-34 and $Cu/ZnO/Al_2O_3$ physical powder mixture (PM), pellet/granule mixture (GM) and dual bed (DB) catalysts to assess their performance. These are all described in depth in section 1.2 of the ESI.†

Characterisation protocols are outlined in section 3 of the ESI.†

Catalytic testing

Bifunctional catalysts were tested for the one-pot conversion of CO_2 to DME in a pressurised, fixed bed continuous flow reactor. The bifunctional catalysts particles (0.300 g, sieved between 300–500 μm) were tested at 260 °C under 40 bar of pressure with a 3 : 1 $H_2 : CO_2$ volumetric mixture that was flowed with a GHSV of 13 000 mL g_{cat}^{-1} h^{-1}. Exit gases were monitored using an online Hiden QGA mass spectrometer. The reactor schematic and further catalytic details are provided in section 2 of the ESI† (Fig. S2 and S3). Catalyst powder was pelletised at 4 tonnes as this pelletising pressure was found to provide a good balance between minimal solid acid framework degradation and maximum gain of desired size fraction (Fig. S4†). Pelletised and crushed catalyst particles were sieved five times as this was found to give

Table 2 Copper and zinc loading of CuZnO/SAPO-*X* (where *X* = 11 or 34) catalysts prepared *via* different synthetic methods

	Cu loading (wt%)		Zn loading (wt%)		Cu/Zn mass ratio	
Synthesis method	−11	−34	−11	−34	−11	−34
ID	13.1	12.5	5.6	5.6	2.3	2.2
OG	13.1	14.8	5.5	5.0	2.4	3.0
DP	10.7	9.3	5.9	4.3	1.8	2.2
Intended	15.4		7.7		2	

superior catalytic performance compared to a singular sieving approach.[38]

Results and discussion

Catalyst characterisation

All the synthesised catalysts contained lower Cu and Zn loadings than intended which was attributed to saturation of the external surfaces. Variations in Cu and Zn loadings occurred primarily due to the synthetic method and to a lesser extent the solid acid itself (Table 2). This agrees with Ahmad *et al.* who found that the choice of synthesis method influenced the CuO and ZnO loadings of Cu–ZnO–Al_2O_3/H-MFI 400 catalysts.[35] CHN analysis has shown that the fresh CuZnO/SAPO-*X* catalysts contained a small amount of residual carbon (<0.3 wt%), with the SAPO-11 catalysts having higher carbon content on average than the SAPO-34 catalysts (Table S1†).

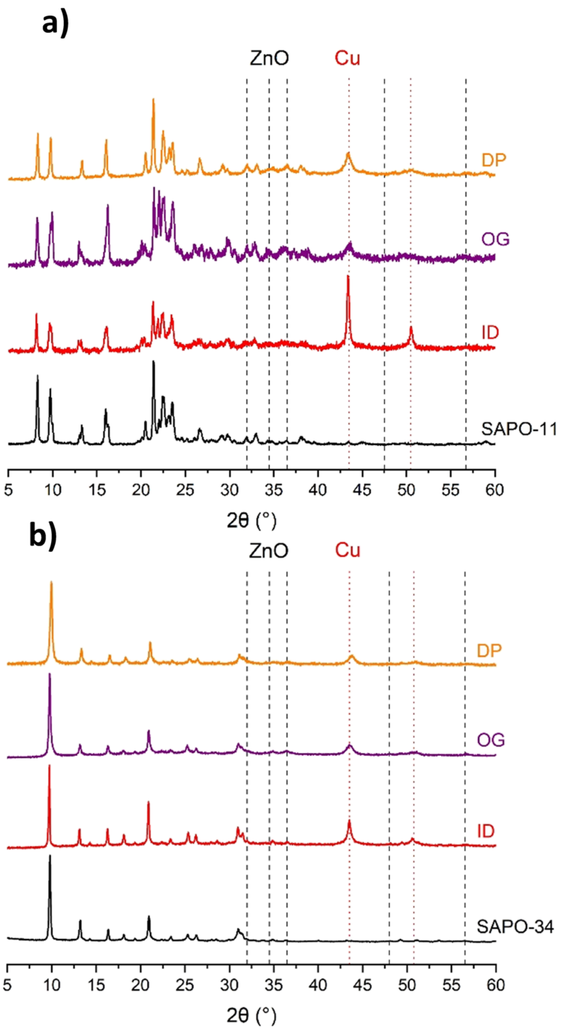

Fig. 2 PXRD patterns of a) CuZnO/SAPO-11 and b) CuZnO/SAPO-34 bifunctional catalysts prepared *via* different methods showing the appearance of Cu and ZnO reflections.

Powder X-ray diffraction (PXRD) confirmed the phase purity of SAPO-11 and SAPO-34 solid acid catalysts as only the AEL and CHA crystalline phases were observed, respectively (Fig. 2).[15,39,40] Impregnation of Cu and Zn onto the SAPO supports gave new peaks at 43 and 51° (111 and 200 planes of metallic Cu)[41,42] and at 32, 34.5, 36.5, 48 and 56.5° (100, 002, 101, 102 and 110 planes of wurtzite ZnO),[43,44] respectively (Fig. S5†). The ZnO peak intensity was noticeably weaker than the Cu, suggesting small ZnO particles were present, in agreement with Tariq *et al.*[31]

Total surface area of the undoped SAPOs was within the expected range (Table S2†).[15,36,37,45] SAPO-11 showed a type IV isotherm with a H4 hysteresis loop indicating micro-mesoporosity (Fig. S6a†) due to interparticle voids caused by an aggregation of SAPO-11 particles rather than due to ordered mesopores within the SAPO-11 framework itself.[46] Lack of significant peaks in the pore size distribution plot has indeed verified that SAPO-11 contains no ordered mesopores. Type I isotherm typical of microporous frameworks with small external surface areas was obtained for SAPO-34 (Fig. S6b†).[46] The overall surface area decreases upon introduction of Cu and Zn (Table S2†), suggesting either the porous SAPO is being diluted by the dense Cu and Zn species, or these species are blocking access to the internal framework of the SAPO support. The synthesised bifunctional catalysts have similar metal loadings, but the decrease in surface area varies significantly between the different synthetic approaches and the solid acid, which suggests that the preparation method and the support itself can impact the size, morphology and distribution of the CuZnO species. The synthetic approach also leads to a decrease in the surface area as is seen for the undoped SAPO-11 ID and SAPO-34 ID catalysts which have undergone the impregnation and drying approach without the deposition of metal (Table S3†). This is due to a combined effect of the subsequent hydrothermal, calcination and reduction steps which have a mild detrimental effect on the crystallinity of the solid acid.

Scanning electron microscopy (SEM) images for the different CuZnO/SAPO systems (Fig. S7†) show spherical SAPO-11 and cubic SAPO-34 crystals with an average size of 10 and 2 μm, respectively. Here the heavier Cu and Zn species appear brighter compared to the SAPO support. As can be seen in Fig. S7,† the synthetic approach has a profound impact on the resulting shape, size, and location of the CuZnO nanoparticles whereas the choice of SAPO support had limited effect. The ID method results in a uniform distribution of irregular nanoparticles across outer crystal faces (Fig. S7a and d†) while the OG approach leads to two distinct types of metallic species: nanoparticles which adhere directly to crystal surfaces and larger particles which appears loosely associated with the crystals (Fig. S7b and e†). The DP method results in coating of the crystals with flocculent metallic species (Fig. S7c and f†).

Transmission electron microscopy (TEM) was performed on both CuZnO/SAPO-11 and CuZnO/SAPO-34 catalysts but only CuZnO/SAPO-34 catalysts will be discussed as the irregular SAPO-11 crystals made it challenging to accurately discern nanoparticles and the support. TEM imaging (Fig. S8†) has verified our SEM findings (Fig. S7†) that the synthesis method plays a key role in the morphology and distribution of the CuZnO nanoparticles. The ID method gives rise to nanoparticles which adhere to the outer crystal faces of SAPO-34 (Fig. S8a†). Previously using SEM for the CuZnO/SAPO-34 OG catalyst, large (~100 nm) CuZnO particles were observed associated with the SAPO-34 and SAPO-11 crystals (Fig. S7b and e†). Using high resolution TEM, it was found that these large particles are in actual fact agglomerates of smaller nanoparticles. OG therefore gives a mixture of nanoparticles which reside on the SAPO-34 crystals as well as agglomerates of nanoparticles that are loosely associated with the SAPO support (Fig. S8b†). The DP method forms large agglomerates of nanoparticles which are loosely affiliated with the cubic SAPO-34 crystals (Fig. S8c†). In terms of nanoparticle size, the OG, ID and DP methods gave an average size of 13, 15 and 20 nm respectively with all methods giving a narrow nanoparticle size distribution (Fig. 3 and S9†).

Ammonia temperature programmed desorption (NH_3-TPD) probed the influence of the synthetic method on acid strength and quantity (Fig. S10 and Table S4†). As expected, the bare SAPO-34 system shows, on average, stronger acid sites, and a greater quantity of acid sites than the SAPO-11. The SAPO-34 appears to have multiple acid sites, as shown by a shoulder peak at 300 °C, and a main peak at 450 °C. In contrast SAPO-11 shows a single feature, centred at 320 °C. The choice of synthetic method has a pronounced effect on acid site strength and quantity of the CuZnO/SAPO-*X* catalysts, and this is independent of the SAPO itself (Fig. S10 and Table S4†). The ID approach creates a range of acid sites and leads to a significant increase in the total quantity of acid sites which is highly desirable for the acid catalysed MeOH dehydration reaction. Baek *et al.* have also reported that the choice of copper acetate precursors used in the ID method leads to a higher number of acid sites in a bifunctional Cu–ZnO/γ-Al_2O_3 catalysts.[33] Navarro-Jaén *et al.* have also reported the appearance of a strongly acidic peak in NH_3-TPD following introduction of CuZnO to SAPO-34 to make a bifunctional catalyst.[29] The OG method creates new weakly acidic sites at the behest of stronger acid sites but the total amount of acid sites remains constant for CuZnO/SAPO-34 OG and increases for CuZnO/SAPO-11 OG. The DP method reduces both the strength and quantity of acid sites, and this is attributed to the degradation of the solid acid framework by the alkaline precipitant which has also been noted by Wang *et al.*[47]

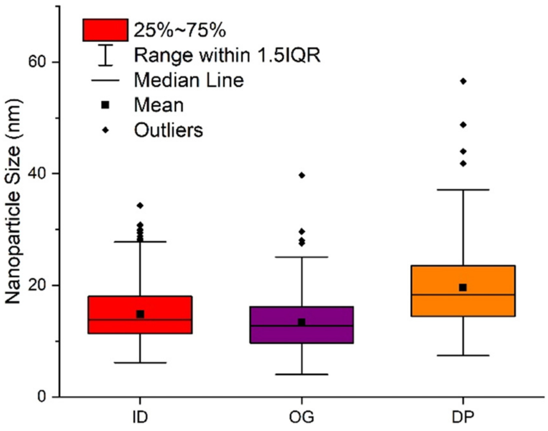

Fig. 3 Nanoparticle size distribution of CuZnO/SAPO-34 catalysts prepared *via* different methods. Results are based on a measurement of 300 nanoparticles.

Cu and Zn K edge X-ray absorption spectroscopy (XAS) spectra for CuZnO/SAPO-11 and CuZnO/SAPO-34 ID, OG and DP catalysts are presented in Fig. S11 and S12 of the ESI.† Linear combination fitting of the X-ray absorption near edge structure (XANES) region (Fig. S11†) has indicated that the Cu in CuZnO/SAPO-11 and CuZnO/SAPO-34 catalysts prepared *via* the ID and DP methods exists mostly as Cu^0 with some being oxidised to Cu^+/Cu^{2+} (Table S5†), whereas the OG catalysts existed in a more oxidised form highlighting once more the impact of synthesis choice. SAPO-34 based catalysts have a marginally lower Cu oxidation states. Based on *in situ* XAS studies of various Cu-based MeOH synthesis catalysts,[48–51] it is highly likely that all the Cu sites are reduced to Cu^0 during the pre-reaction *in situ* reduction in pure H_2 at 300 °C. The Zn oxidation state for all the catalysts was determined as +2 and neither the synthetic method nor the solid acid appeared to have any impact on the Zn centre (Fig. S12 and Table S5†).

Extended X-ray absorption fine structure (EXAFS) fitting has shown that the Cu sites in catalysts prepared *via* ID and DP methods are mostly Cu^0, whereas those prepared *via* OG method are a mixture of Cu^0 and Cu_2O/CuO (Table 3 and Fig. S13†). The OG catalysts are more sensitive to oxidation and this is especially evident for the CuZnO/SAPO-11 OG catalyst in which the Cu exists mostly as Cu_2O/CuO rather than Cu^0. These catalysts have Cu–Cu coordination number significantly lower than 12 which would be expected for bulk Cu and this phenomenon has also been witnessed by Sun *et al.* for ultrafine Cu/ZnO/Al_2O_3 catalysts prepared *via* the OG method.[52] This is due to oxidation of Cu centres as well as the possibility that some Cu exist in the amorphous state with poorly defined Cu–Cu coordination. The Zn exists solely as ZnO and there are only minor differences between the Zn–O coordination number with no clear trend witnessed (Table S6 and Fig. S14†). The synthetic method nor the solid acid have any appreciable impact on the Zn site. Wavelet transformation of the EXAFS region was performed to resolve any possible contributions of backscattering atoms which could overlap in the *R* space due to similar bond lengths. No additional backscattering atoms were identified and only hotspots consistent with the anticipated Cu–O, Cu–Cu, Zn–O and Zn–Zn were observed (Fig. S15–S18†). Wavelet analysis has shown no sign of alloying between Cu and Zn.

Table 3 EXAFS fitting for Cu K-edge data of CuZnO/SAPO-*X* (where *X* = 11 or 34) catalysts prepared *via* the ID, OG and DP synthetic methods

Synthesis method	Scattering path	N		$2\sigma^2$ (Å^2)		R (Å)		E_f (eV)		R factor	
		−11	−34	−11	−34	−11	−34	−11	−34	−11	−34
ID	Cu–Cu	6.2(3)	6.7(2)	0.0085(4)	0.0091(3)	2.543(9)	2.542(5)	5(1)	4(1)	0.009	0.003
	Cu–O	1.4(2)	1.0(1)	0.006(2)	0.006(2)	1.89(2)	1.87(1)				
OG	Cu–Cu	0.4(2)	4.5(2)	0.004(4)	0.0089(4)	2.55(3)	2.549(8)	10(2)	5(1)	0.035	0.007
	Cu–O	3.0(3)	1.4(1)	0.005(1)	0.007(2)	1.94(2)	1.87(1)				
DP	Cu–Cu	6.2(2)	6.2(2)	0.0095(3)	0.0091(3)	2.543(5)	2.545(6)	4(1)	4(1)	0.003	0.004
	Cu–O	1.0(1)	1.1(1)	0.005(2)	0.006(2)	1.87(1)	1.86(1)				

Amplitude reduction factor of 0.886 was determined from fitting of Cu^0 with fixed CN of 12. A fit employing only the Cu–O path was attempted for the CuZnO/SAPO-11 OG catalyst but this provided an inferior fit compared to fitting both Cu–Cu and Cu–O paths. Values in brackets indicate error (±) in the last reported significant figure.

X-ray photoelectron spectroscopy (XPS) spectra of all the bifunctional catalysts showed shake up satellites (peaks 3–5) in the Cu $2p_{3/2}$ region (Fig. S19†). These are indicative of ground state d^9 Cu^{2+} species.[53,54] Fitting of the main Cu $2p_{3/2}$ peak has shown that the peak is caused by Cu^{2+} (933.5 eV, peak 2) and Cu^+/Cu^0 species (932.4 eV, peak 1). Due to spectral overlap of the Cu $2p_{3/2}$ peak, it is not possible to discern whether peak 1 is caused by Cu^+ or Cu^0 species but through examination of the Cu $L_3M_{4,5}M_{4,5}$ spectrum it is usually possible to resolve the two.[53,54] Unfortunately, for all catalysts other than the DP catalysts, the Cu $L_3M_{4,5}M_{4,5}$ spectrum showed no discernible peaks (Fig. S20†) and as such it is not possible to conclusively verify whether peak 1 is caused by Cu^+ or Cu^0 species. Based on the XPS and XAFS results it can thus be stated that the Cu exists as a mixture of Cu^0 and Cu_2O/CuO. In line with previous reports,[50,55] it is possible that the Cu exists as a metallic core – oxidised shell structure. This explains why the surface-sensitive XPS technique predicts higher Cu oxidation compared to the bulk-sensitive XAFS technique. The CuZnO/SAPO-11 catalysts showed on average higher peak area percentages of peaks 2–5 compared to peak 1 (Fig. S21 and Table S7†) which would indicate that the CuZnO/SAPO-11 catalysts suffered from greater Cu oxidation (Fig. 4) which is consistent with the XANES analysis (Table S5†). Examination of the Zn 2p region provided limited information due to a statistically insignificant difference between the binding energy of Zn^0 and Zn^{2+} species. However, it is possible to resolve the two species *via* interrogation of the Zn $L_3M_{4,5}M_{4,5}$ spectrum (Fig. S22†).[53] For the OG and DP catalysts the Zn $L_3M_{4,5}M_{4,5}$ Auger peaks were centred around 988 eV which is consistent with ZnO. Interestingly, catalysts prepared *via* the ID method had the Zn Auger peak shifted to slightly lower kinetic energy and appeared at approximately 987 eV. No peak was witnessed at 992 eV for any of the catalysts which indicates a lack of Zn metal. This is consistent with XAFS analysis and shows that Zn exists solely as ZnO.

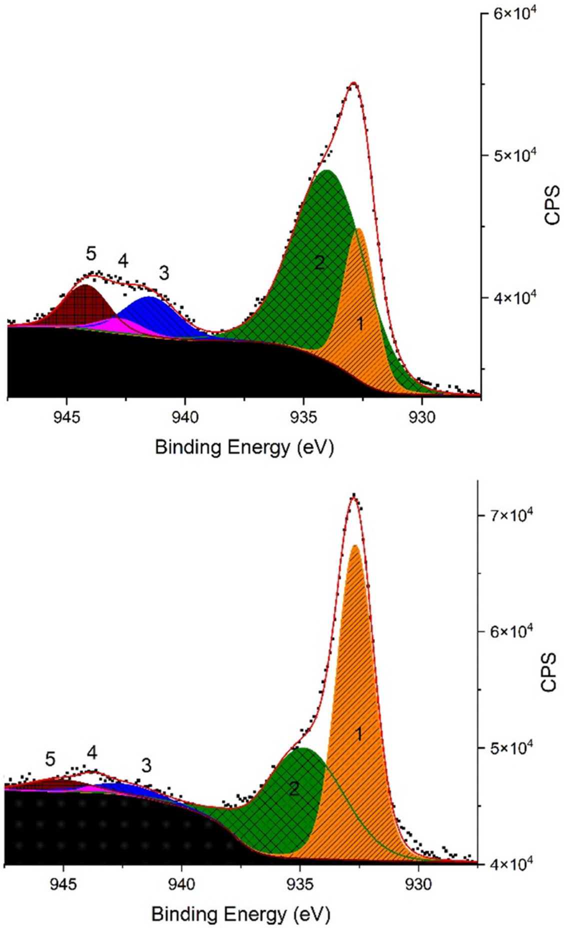

Fig. 4 Curved-fitted Cu $2p_{3/2}$ XPS spectra of top) CuZnO/SAPO-11 ID and bottom) CuZnO/SAPO-34 ID catalysts. Peak 1 is due to Cu^+/Cu^0 and peaks 2–5 are due to Cu^{2+}.

Catalytic activity

All the CuZnO/SAPO-*X* catalysts were active for the one-pot conversion of CO_2 to DME, showing CO_2 conversions between 5 and 17% (Table 4). For the cascade reaction to proceed and produce DME, the redox active site must firstly activate and hydrogenate the CO_2 molecule to form a MeOH intermediate. It was speculated that the overall activity of the bifunctional catalysts relies on the synergy between the Cu and ZnO sites as the Cu–ZnO interfacial region is often considered to be the active site for MeOH synthesis.[56–59] To test this

Table 4 Catalytic performance of bifunctional CuZnO/SAPO-*X* (where *X* = 11 or 34) catalysts compared to physical mixture catalysts. Conditions: 260 °C, 40 bars, 13 000 mL g^{-1} h^{-1} GHSV, 3 : 1 $H_2 : CO_2$ volumetric ratio

	CO_2 conversion (%)		CO selectivity (%)		MeOH selectivity (%)		DME selectivity (%)		CO yield (%)		DME yield (%)	
Catalyst	−11	−34	−11	−34	−11	−34	−11	−34	−11	−34	−11	−34
CuZnO/SAPO-*X* ID	4.7	8.1	0	0	32	20	68	80	0.0	0.0	3.2	6.5
CuZnO/SAPO-*X* OG	14	12	14	30	19	15	67	55	2.0	3.6	9.4	6.6
CuZnO/SAPO-*X* DP	17	13	40	40	36	35	24	25	6.8	5.2	4.1	3.3
$Cu/ZnO/Al_2O_3$ + SAPO-*X* PM	23	18	42	39	14	13	44	48	9.7	7.0	10	8.6
$Cu/ZnO/Al_2O_3$ + SAPO-*X* GM	26	21	44	43	13	12	43	45	11	9.0	11	9.5
$Cu/ZnO/Al_2O_3$ + SAPO-*X* DB	18	11	42	46	13	11	45	43	7.6	5.1	8.1	4.7

DB is dual bed, GM is granule/pellet physical mixture, PM is powder physical mixture. Low DME selectivity of DP catalysts is attributed to degradation of the solid acid framework. Average carbon mass balance of 97%.

hypothesis, Cu/SAPO-*X* and ZnO/SAPO-*X* powders were physically mixed, pelletised and tested. No activity was witnessed for these catalysts showing that the mere presence of the two metals is insufficient and that proximity between the Cu and ZnO sites plays a key role in catalytic activity. Additional testing found negligible catalytic activity of the Cu/SAPO-*X*, ZnO/SAPO-*X* and SAPO-*X* individual components. Non-deposited CuZnO prepared by the ID method also showed significantly reduced MeOH and DME production, compared to the deposited CuZnO/SAPO species. This shows that dispersing the CuZnO species on to a support is crucial for designing the bifunctional catalysts (Table S9†). For the one-pot conversion of CO_2 to DME, a bifunctional catalyst thus requires synergistically active and well-dispersed CuZnO sites for the initial hydrogenation of CO_2, and sufficient acid sites of the right strength to selectively dehydrate the MeOH intermediate to DME.

Of the three active catalyst sets, catalysts produced *via* the ID method had the highest DME selectivity and no CO was detected (Table 4) during the reaction showing a significant suppression of the RWGS reaction. The most striking difference between the catalysts produced using the three different methods was the acid site strength and quantity as well as the location and distribution of the CuZnO nanoparticles. A strong negative correlation was found between acid site quantity and CO selectivity, with the CuZnO/SAPO-*X* ID catalysts showing the lowest CO selectivity and highest acid site quantity. A linear correlation was obtained by plotting the total integrated area of the NH_3-TPD signal (acid site quantity) for the CuZnO/SAPO-*X* catalysts against their CO selectivity (Fig. S23†). The DME selectivity showed a positive correlation to acid site quantity. This demonstrates that by tailoring the acid site quantity of bifunctional catalysts it is possible to optimise the DME and CO selectivity during one-pot conversion of CO_2. We hereby propose a water inhibition effect as a possible hypothesis to explain the relationship between acid site abundance and CO-formation inhibition. Catalysts with stronger and more abundant acid sites catalyse the dehydration of the intermediate MeOH to a greater extent which leads to significant production of water. This increase in localised water concentration can help to shift the thermodynamic equilibrium towards the conversion of CO into CO_2 *via* the WGS reaction (eqn (5)). This therefore helps to significantly suppress the RWGS reaction which leads to low CO levels that are below the detectable level of our mass spectrometer instrument. The CuZnO/SAPO-*X* ID catalysts contain the most abundant acid sites which led to significant water production (Table S10†) which resulted in the lowest CO selectivity observed. Further experimental validation through *operando* studies, coupled with computational calculations are required to ascertain whether this proposed localised water inhibition hypothesis vindicates the relationship between active site abundance and CO-formation suppression. Unfortunately, an increase in localised water concentration also shifts the equilibrium away from MeOH formation which reduces the CO_2 conversion and explains the lower CO_2 conversions for the ID catalysts. As such, there is the commonly encountered trade-off between activity and selectivity. Nevertheless, from an industrial perspective, high selectivity to DME is preferred as this significantly reduces toxic CO by-product formation and it is possible to increase overall conversions by using approaches such as recycling loops.

The secondary difference between the catalysts produced *via* the three methods was the proximity between the CuZnO nanoparticles and the SAPO supports. Although electron microscopy enables a visual assessment of this, it is not possible to use it to calculate a bulk-representative average distance between the nanoparticles and the support. To overcome this challenge and understand whether there is a link between site proximity and selectivity, a follow-up study was conducted whereby the distance between the redox and acid components was varied on the macroscopic scale. An optimised $Cu/ZnO/Al_2O_3$ MeOH synthesis catalyst and the SAPO-*X* solid acid catalysts were mixed in different manners to obtain varying degrees of proximity between the two functionalities. A dual bed (DB), granule mixing (GM) and powder mixing (PM) were used with the dual bed having the largest spatial separation between the two and powder mixing the smallest spatial site separation. Table 4 shows that CO selectivity decreases marginally with an increase in proximity between the two components which is in line with previous reports.[25,26] The water production also increases with an increase in proximity (Table S10†) which is in line with our proposed water inhibition effect and explains the lower CO selectivity. However, the CO selectivity is still high and the influence of proximity on CO selectivity is minor. This demonstrates that the water inhibition effect is a very localised phenomenon and requires direct contact between the CuZnO nanoparticles and the SAPO support which demonstrates the advantage of bifunctional catalysts over a physical mixture of two distinct catalysts. The CuZnO/SAPO-34 ID catalyst has both a high abundance of acid sites and the CuZnO nanoparticles are deposited directly onto the SAPO support surface which results in highly efficient suppression of the RWGS reaction.

Comparing SAPO-11 and SAPO-34, it can be seen that on average, the CuZnO/SAPO-34 catalysts produced *via* all methods tend to give higher DME selectivity compared to their SAPO-11 equivalents. This is attributed to the stronger and more abundant acid sites of SAPO-34 compared to SAPO-11 (Fig. S10†) which results in rapid MeOH dehydration. This is further shown by the fact that the CuZnO/SAPO-11 catalysts tend to give higher MeOH selectivity compared to their SAPO-34 equivalents as the MeOH is clearly not as rapidly dehydrated (Table 4).

Catalyst stability

A time-on-stream stability study was conducted to assess the catalytic performance of the active bifunctional catalysts for the one-pot DME formation approach. Mirroring the trends witnessed in Table 4, the DP catalysts consistently gave the highest CO_2 conversions and ID catalysts the lowest (Fig. 5). Initial CO_2 conversions were similar between analogous CuZnO/SAPO-11 and CuZnO/SAPO-34 catalysts (Fig. 5 and S24†), but as the reaction progressed the CuZnO/SAPO-34 catalysts retained their activity while the CuZnO/SAPO-11 catalysts showed minor, although appreciable, decline in CO_2 conversions. SAPO-34 therefore appears to be a better solid acid of choice for creating stable bifunctional catalysts for one-pot conversion of CO_2 to DME. Exit gas was collected at 15, 45, 140, 240 and 420 minutes during the stability study and offline GC and GC–MS analysis was conducted. GC analysis has confirmed that MeOH and DME were the only hydrocarbon products present in the gas stream. It was also found that the GC determined DME selectivity matched well the MS determined DME selectivity for the CuZnO/SAPO-34 ID catalyst (Fig. S25†) thus validating its high DME selectivity. GC–MS has found fragment ions peaks which could be attributed to MeOH and DME (Fig. S26†), but fragment peaks belonging to ethene or propene could not be found showing no significant conversion of CO_2 to olefins. As seen in Fig. 5, the ID catalysts show a minor initial decrease in DME selectivity, but these plateau after 2 hours. The OG and DP catalysts on the other hand show an increase in both DME and MeOH selectivity as a function of time and this is concomitant with a decrease in CO selectivity. The decrease in CO selectivity with time is witnessed for all OG and DP catalysts. The time-on-stream study was also performed using a commercially available Cu-based MeOH synthesis catalyst and over the period of 7 hours, the CO_2 conversion and CO selectivity remained constant at 22 and 60% respectively (Fig. S27†) which is in-line with previously reported results.[60] This suggests that the decrease in CO selectivity witnessed herein is a real phenomenon and not a function of our experimental conditions. TEM images of spent CuZnO/SAPO-34 OG and DP catalysts (Fig. S28†) show the CuZnO nanoparticles (redox species) are more closely associated with the SAPO-34 surface (acid sites) than in the as-synthesised systems. This could explain the reduced CO selectivity with time as the increased proximity may increase the efficiency of the hypothesised water inhibition effect. An alternate explanation is that the CO_2 hydrogenation and RWGS reactions take place over different active sites in these bifunctional catalysts and that the site responsible for RWGS deactivates rapidly. The exact reason for this decrease in CO production with time is not yet fully understood and future *operando* characterisation studies of these catalysts will be required to understand this behaviour.

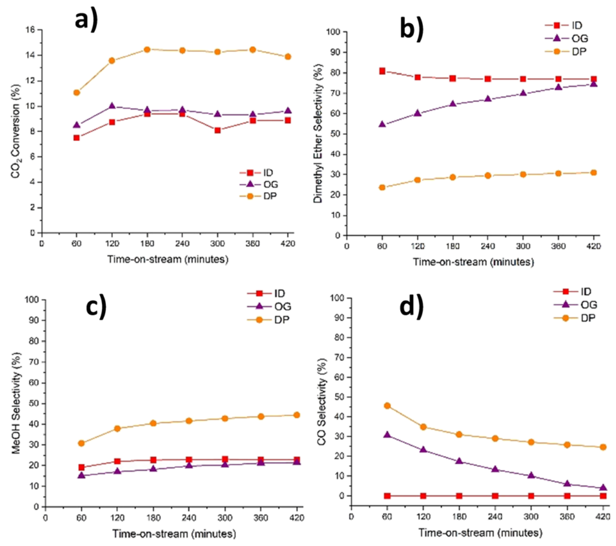

Fig. 5 Catalytic performance of CuZnO/SAPO-34 catalysts synthesised *via* the ID, OG and DP methods as a function of time-on-stream. a) CO_2 conversion b) DME selectivity c) MeOH selectivity d) CO selectivity. Conditions: 260 °C, 40 bars, 13 000 mL g^{-1} h^{-1} GHSV, 3 : 1 $H_2 : CO_2$ volumetric ratio. Average carbon mass balance of 97%.

Further characterisation of spent catalysts used for the above time-on-stream stability was performed to better understand structural changes triggered by the catalysis. XRD characterisation has shown that the OG and DP catalysts suffer from Cu sintering due to an increase in the intensity of the Cu 111 peak (Fig. S29†). The ID catalysts on the other hand do not appear to suffer from sintering to the same degree as the intensity and line width of the Cu 111 peak appears to remain unchanged during the reaction. Indeed, TEM analysis of spent CuZnO/SAPO-34 OG and DP catalysts has shown that the average nanoparticle size has increased from 13 & 20 to 15 and 23 nm, respectively. The average nanoparticle size of the CuZnO/SAPO-34 ID catalyst on the other hand has decreased from 15 to 11 nm during the reaction (Fig. S30†). BET analysis of spent samples has curiously shown that the surface area of the spent pelletised CuZnO/SAPO-34 ID, OG and DP catalyst has increased marginally during the reaction (Table S11†). This could possibly be explained by the agglomeration of nanoparticles which leads to a reduction in the surface coverage of the SAPO-34 support which improves the access of guest species to the internal cage network of the solid acid. The CuZnO/SAPO-11 catalysts on the other hand appear to suffer from a marginal reduction in their surface area during the reaction. CHN analysis has found that both catalyst sets suffer from very marginal coking (<0.1 wt%) during the reaction which can contribute to deactivation (Table S1†). This level of coking is minor and significantly less than what is usually seen for SAPO-11 and SAPO-34 during MeOH dehydration, where the catalysts usually gain 1 & 10 wt% of carbon during the reaction, respectively.[15] On average, the CuZnO/SAPO-11 catalysts gained more coke during the reaction compared to their SAPO-34 analogues. The higher level of coking of SAPO-11 would explain why its surface area decreased more significantly compared to SAPO-34. The elevated carbon gain could also indicate why SAPO-11 catalysts appear to deactivate more rapidly compared to their SAPO-34 analogues. There is no clear trend between coking and the catalyst synthesis method.

Synthesis–structure–property correlations (SSPCs)

The ID, OG and DP methods give rise to Cu–ZnO synergy which enables the bifunctional catalyst to perform the initial hydrogenation of the CO_2 molecule and endows the catalyst with overall activity. The synthesis method influences the location and distribution of the CuZnO nanoparticles which can impact the grafting of the metal particles to the SAPO support. The ID method resulted in CuZnO nanoparticles being deposited solely on the SAPO-*X* solid acid support, whilst the OG and DP methods result in a mixture of supported nanoparticles and unsupported nanoparticle agglomerates that are loosely associated with the SAPO crystals. More importantly, the synthesis method significantly impacted the total quantity of acid sites with the ID method giving rise to high abundance of acid sites whilst the DP method degrades the SAPO framework resulting in low abundance of acid sites, with the OG method showing an intermediate number of acid sites. We believe that high acid site abundance leads to more extensive dehydration of the intermediate MeOH which results in high DME selectivity. The higher levels of MeOH dehydration result in greater water production, which has a positive side benefit in suppressing the parasitic RWGS reaction thus lowering CO production significantly. Stability can be tuned by the synthesis method and depositing the nanoparticles directly onto the SAPO helps anchoring them, hindering agglomeration, thus retaining the active sites and the activity.

In this work, the CuZnO/SAPO-34 catalyst produced *via* the impregnation and drying method is the most promising for the selective one-pot conversion of CO_2 to DME. CuZnO nanoparticles are anchored directly onto the SAPO-34 solid acid support using the ID approach which affords synergy between the Cu and ZnO species. Furthermore, the ID synthesis method yields a bifunctional catalyst with both a high surface area and high number of moderate strength Brønsted acid sites. Overall, these beneficial structural features obtained *via* the ID method result in modest CO_2 conversions, high stability, exceptional DME selectivity and most importantly significant suppression of the CO-producing RWGS reaction due to the theorised localised water inhibition effect. Compared to other similar catalytic systems used for the one-pot synthesis of DME, our catalyst shows amongst the highest DME selectivity and lowest CO formation (Table S13†). This is highly desirable for industrial applications as on large scale this not only reduces overall waste, but also the formation of toxic by-products which is in line with green chemistry principles. Although the CO_2 conversions are modest for the ID catalysts, there exist scope in both laboratory and industrial practice to take advantage of the high DME selectivity and boost CO_2 conversions through further catalytic modification and reactor engineering.

Conclusions

Replacement of fossil fuels used for long-haul marine transport with sustainable alternatives will be critical in ensuring the shipping sector curbs its emission significantly and achieves carbon neutrality. In this vein, we have developed an array of CuZnO/SAPO-11 and CuZnO/SAPO-34 bifunctional catalysts for the one-pot conversion of CO_2 to the sustainable alternative fuel, DME. We have developed the catalysts using a range of approaches to develop synthesis–structure–property correlations (SSPCs) which can guide the design of future catalysts for this reaction. We found that the choice of synthesis method had a profound impact on the morphology and location of CuZnO nanoparticles and on the total quantity of acid sites of the bifunctional catalyst. Catalysts prepared *via* the impregnation and drying, oxalate gel deposition precipitation and deposition precipitation approaches were active for one-pot CO_2 to DME conversion and this was attributed to proximity between Cu and ZnO sites which can promote synergy enhancements for the initial conversion of CO_2 to MeOH. SAPO-34 based catalysts had higher DME selectivity and stability than their SAPO-11 analogues. The CuZnO/SAPO-34 catalyst prepared *via* the impregnation and drying method had the most promising catalytic performance, reaching a DME selectivity of 80%

without the production of any detectable CO. The superior performance is attributed to the most abundant acid sites of all the catalysts as well as proximity between the CuZnO nanoparticles and Brønsted acid sites of the SAPO-34 support. This results in facile dehydration of the intermediate MeOH leading to an increase in localised water production which can supress the CO-forming RWGS reaction.

Author contributions

MGW – conceptualization, data curation, formal analysis, investigation, validation, visualisation, writing – original draft, review & editing. MEP – conceptualization, data curation, formal analysis, investigation, methodology, writing – review & editing. EB – data curation, formal analysis, investigation. SK – conceptualization, writing – review & editing. LMA & RR – conceptualization, funding acquisition, project administration, resources, supervision, writing – review & editing.

Conflicts of interest

There are no conflicts to declare.

Acknowledgements

MGW would like to thank the University of Southampton and the Southampton Marine and Maritime Institute for their funding. We would also like to thank: HarwellXPS for XPS data collection which was performed at EPSRC National Facility for XPS ('HarwellXPS'), operated by Cardiff University and UCL, under contract No. PR16195, UK Catalysis Hub block allocation group for XAFS beamtime (SP29271), Dr Matthew Cooper at the School of Ocean and Earth Science at the University of Southampton for their help with ICP-MS analysis, Patricia Goggin, Regan Doherty and the wider team at the Biological Imaging Unit at the University Hospital Southampton for their help with TEM imaging and Professor John Langley and Dr Julie Herniman for their help with GC–MS analysis.

Notes and references

1 P. Balcombe, J. Brierley, C. Lewis, L. Skatvedt, J. Speirs, A. Hawkes and I. Staffell, *Energy Convers. Manage.*, 2019, **182**, 72–88.

2 A. Al-Enazi, E. C. Okonkwo, Y. Bicer and T. Al-Ansari, *Energy Rep.*, 2021, **7**, 1962–1985.

3 H. Stančin, H. Mikulčić, X. Wang and N. Duić, *Renewable Sustainable Energy Rev.*, 2020, **128**, 109927.

4 G. A. Olah, A. Goeppert and G. K. S. Prakash, *J. Org. Chem.*, 2009, **74**, 487–498.

5 J. Sun, G. Yang, Y. Yoneyama and N. Tsubaki, *ACS Catal.*, 2014, **4**, 3346–3356.

6 W. Alharbi, E. F. Kozhevnikova and I. V. Kozhevnikov, *ACS Catal.*, 2015, **5**, 7186–7193.

7 A. Álvarez, A. Bansode, A. Urakawa, A. V. Bavykina, T. A. Wezendonk, M. Makkee, J. Gascon and F. Kapteijn, *Chem. Rev.*, 2017, **117**, 9804–9838.

8 Dimethyl Ether Market Share, Size, Trends, Industry Analysis Report, By Raw Material (Fossil Fuel Based, Bio-based); By Application; By Region; Segment Forecast, 2022–2030, **https://www.polarismarketresearch.com/industry-analysis/dimethyl-ether-market**, (accessed 29 August 2023).

9 E. Catizzone, G. Bonura, M. Migliori, F. Frusteri and G. Giordano, *Molecules*, 2018, **23**, 31.

10 N. Mota, E. M. Ordoñez, B. Pawelec, J. L. G. Fierro and R. M. Navarro, *Catalysts*, 2021, **11**, 411.

11 E. S. Yoon and C. Han, *Comput.-Aided Chem. Eng.*, 2009, **27**, 169–175.

12 M. Kosari, A. M. H. Lim, Y. Shao, B. Li, K. M. Kwok, A. M. Seayad, A. Borgna and H. C. Zeng, *J. Mater. Chem. A*, 2023, **11**, 1593–1633.

13 P. Yan, H. Peng, J. Vogrin, H. Rabiee and Z. Zhu, *J. Mater. Chem. A*, 2023, **11**, 17938–17960.

14 U. Olsbye, S. Svelle, M. Bjrgen, P. Beato, T. V. W. Janssens, F. Joensen, S. Bordiga and K. P. Lillerud, *Angew. Chem., Int. Ed.*, 2012, **51**, 5810–5831.

15 W. Dai, X. Wang, G. Wu, N. Guan, M. Hunger and L. Li, *ACS Catal.*, 2011, **1**, 292–299.

16 H. Bateni and C. Able, *Catal. Ind.*, 2019, **11**, 7–33.

17 N. Khandan, M. Kazemeini and M. Aghaziarati, *Appl. Catal., A*, 2008, **349**, 6–12.

18 M. E. Potter, *ACS Catal.*, 2020, **10**, 9758–9789.

19 A. M. Prakash, S. V. V. Chilukuri, R. P. Bagwe, S. Ashtekar and D. K. Chakrabarty, *Microporous Mater.*, 1996, **6**, 89–97.

20 W. Dai, W. Kong, G. Wu, N. Li, L. Li and N. Guan, *Catal. Commun.*, 2011, **12**, 535–538.

21 Toyo DME Technology, **https://toyo-eng.com/wordpress/wp-content/uploads/2022/12/TOYO_DME.pdf**, (accessed 30 October 2023).

22 Dimethyl Ether, **https://grillo.de/en/products/chemical-products/sulphates-sulphites/dimethyl-ether-dme-grillo-one/**, (accessed 30 October 2023).

23 International DME Assosciation, **https://www.aboutdme.org**, (accessed 30 October 2023).

24 Commercial Operations Commence at Methanol / Dimethyl Ether Plant in Trinidad and Tobago, **https://www.mhi.com/news/210119.html**, (accessed 30 October 2023).

25 P. Gao, S. Li, X. Bu, S. Dang, Z. Liu, H. Wang, L. Zhong, M. Qiu, C. Yang, J. Cai, W. Wei and Y. Sun, *Nat. Chem.*, 2017, **9**, 1019–1024.

26 L. Yao, X. Shen, Y. Pan and Z. Peng, *Energy Fuels*, 2020, **34**, 8635–8643.

27 H. Bahruji, R. D. Armstrong, J. Ruiz Esquius, W. Jones, M. Bowker and G. J. Hutchings, *Ind. Eng. Chem. Res.*, 2018, **57**, 6821–6829.

28 K. S. Yoo, J. H. Kim, M. J. Park, S. J. Kim, O. S. Joo and K. D. Jung, *Appl. Catal., A*, 2007, **330**, 57–62.

29 S. Navarro-Jaén, M. Virginie, J. Thuriot-Roukos, R. Wojcieszak and A. Y. Khodakov, *J. Mater. Sci.*, 2022, **57**, 3268–3279.

30 X. Cui, W. Yan, H. Yang, Y. Shi, Y. Xue, H. Zhang, Y. Niu, W. Fan and T. Deng, *ACS Sustainable Chem. Eng.*, 2021, **9**, 2661–2672.

31 A. Tariq, J. R. Esquius, T. E. Davies, M. Bowker, S. H. Taylor and G. J. Hutchings, *Top. Catal.*, 2021, **64**, 965–973.

32 G. R. Moradi, S. Nosrati and F. Yaripor, *Catal. Commun.*, 2007, **8**, 598–606.

33 S. C. Baek, S. H. Kang, J. W. Bae, Y. J. Lee, D. H. Lee and K. Y. Lee, *Energy Fuels*, 2011, **25**, 2438–2443.

34 Q. Ge, Y. Huang, F. Qiu and S. Li, *Appl. Catal., A*, 1998, **167**, 23–30.

35 R. Ahmad, D. Schrempp, S. Behrens, J. Sauer, M. Döring and U. Arnold, *Fuel Process. Technol.*, 2014, **121**, 38–46.

36 K. V. V. S. B. S. R. Murthy, S. J. Kulkarni and S. K. Masthan, *Microporous Mesoporous Mater.*, 2001, **43**, 201–209.

37 M. E. Potter, L. M. Armstrong and R. Raja, *Catal. Sci. Technol.*, 2018, **8**, 6163–6172.

38 S. Kyrimis, K. E. Rankin, M. E. Potter, R. Raja and L. M. Armstrong, *Adv. Powder Technol.*, 2023, **34**, 103932.

39 W. Dai, G. Wu, L. Li, N. Guan and M. Hunger, *ACS Catal.*, 2013, **3**, 588–596.

40 P. Mériaudeau, V. A. Tuan, V. T. Nghiem, S. Y. Lai, L. N. Hung and C. Naccache, *J. Catal.*, 1997, **169**, 55–66.

41 Y. Sun, L. Xu, Z. Yin and X. Song, *J. Mater. Chem. A*, 2013, **1**, 12361–12370.

42 B. Kumar, S. Saha, M. Basu and A. K. Ganguli, *J. Mater. Chem. A*, 2013, **1**, 4728–4735.

43 F. Rong, J. Zhao, P. Su, Y. Yao, M. Li, Q. Yang and C. Li, *J. Mater. Chem. A*, 2015, **3**, 4010–4017.

44 Y. V. Kaneti, Q. M. D. Zakaria, Z. Zhang, C. Chen, J. Yue, M. Liu, X. Jiang and A. Yu, *J. Mater. Chem. A*, 2014, **2**, 13283–13292.

45 M. E. Potter, M. E. Cholerton, J. Kezina, R. Bounds, M. Carravetta, M. Manzoli, E. Gianotti, M. Lefenfeld and R. Raja, *ACS Catal.*, 2014, **4**, 4161–4169.

46 M. Thommes, K. Kaneko, A. V. Neimark, J. P. Olivier, F. Rodriguez-Reinoso, J. Rouquerol and K. S. W. Sing, *Pure Appl. Chem.*, 2015, **87**, 1051–1069.

47 G. Wang, L. Zeng, J. Cao, F. Liu, Q. Lin, Y. Yi and H. Pan, *Microporous Mesoporous Mater.*, 2019, **284**, 133–140.

48 B. S. Clausen and H. Topsøe, *Catal. Today*, 1991, **9**, 189–196.

49 J. D. Grunwaldt, A. M. Molenbroek, N. Y. Topsøe, H. Topsøe and B. S. Clausen, *J. Catal.*, 2000, **194**, 452–460.

50 D. Grandjean, V. Pelipenko, E. D. Batyrev, J. C. Van Den Heuvel, A. A. Khassin, T. M. Yurieva and B. M. Weckhuysen, *J. Phys. Chem. C*, 2011, **115**, 20175–20191.

51 N. J. Divins, D. Kordus, J. Timoshenko, I. Sinev, I. Zegkinoglou, A. Bergmann, S. W. Chee, S. Widrinna, O. Karslıoğlu, H. Mistry, M. Lopez Luna, J. Q. Zhong, A. S. Hoffman, A. Boubnov, J. A. Boscoboinik, M. Heggen, R. E. Dunin-Borkowski, S. R. Bare and B. R. Cuenya, *Nat. Commun.*, 2021, **12**, 1435.

52 Q. Sun, Y. L. Zhang, H. Y. Chen, J. F. Deng, D. Wu and S. Y. Chen, *J. Catal.*, 1997, **167**, 92–105.

53 M. C. Biesinger, L. W. M. Lau, A. R. Gerson and R. S. C. Smart, *Appl. Surf. Sci.*, 2010, **257**, 887–898.

54 M. C. Biesinger, *Surf. Interface Anal.*, 2017, **49**, 1325–1334.

55 T. Ghodselahi, M. A. Vesaghi, A. Shafiekhani, A. Baghizadeh and M. Lameii, *Appl. Surf. Sci.*, 2008, **255**, 2730–2734.

56 M. Behrens, F. Studt, I. Kasatkin, S. Kühl, M. Hävecker, F. Abild-Pedersen, S. Zander, F. Girgsdies, P. Kurr, B. L. Kniep, M. Tovar, R. W. Fischer, J. K. Nørskov and R. Schlögl, *Science*, 2012, **336**, 893–897.

57 S. Kattel, P. J. Ramírez, J. G. Chen, J. A. Rodriguez and P. Liu, *Science*, 2017, **355**, 1296–1299.

58 S. Kuld, M. Thorhauge, H. Falsig, C. F. Elkjaer, S. Helveg, I. Chorkendorff and J. Sehested, *Science*, 2016, **352**, 969–974.

59 P. Amann, B. Klötzer, D. Degerman, N. Köpfle, T. Götsch, P. Lömker, C. Rameshan, K. Ploner, D. Bikaljevic, H.-Y. Wang, M. Soldemo, M. Shipilin, C. M. Goodwin, J. Gladh, J. H. Stenlid, M. Börner, C. Schlueter and A. Nilsson, *Science*, 2022, **376**, 603–608.

60 P. Gao, F. Li, L. Zhang, N. Zhao, F. Xiao, W. Wei, L. Zhong and Y. Sun, *J. CO2 Util.*, 2013, **2**, 16–23.